DFTT 78/95
Cavendish–HEP–95/17
November 1995
Revised February 1996

Standard Model Higgs boson production and hard photon radiation in $e^+e^- \to \mu^+\mu^- b\bar{b}\gamma$ events at LEP II and Next Linear Collider

Stefano Moretti[1]

Dipartimento di Fisica Teorica, Università di Torino,
and I.N.F.N., Sezione di Torino,
Via Pietro Giuria 1, 10125 Torino, Italy.

Cavendish Laboratory, University of Cambridge,
Madingley Road, Cambridge, CB3 0HE, United Kingdom.

Abstract

We study at LEP II and Next Linear Collider energies Higgs production via the bremsstrahlung channel $e^+e^- \to ZH$, with $Z \to \mu^+\mu^-$ and $H \to b\bar{b}$, and the corresponding irreducible background, in presence of hard photon radiation, both from the initial and the final state. We carry out an analysis that includes the computation of all the relevant contributions to the complete tree–level matrix element for $e^+e^- \to \mu^+\mu^- b\bar{b}\gamma$ and makes use of the one at leading order $e^+e^- \to \mu^+\mu^- b\bar{b}$ interfaced with electron structure functions. We concentrate on the case of mass degeneracy $M_H \approx M_Z$, for which next–to–leading electromagnetic contributions can modify the content of $b\bar{b}$–pairs coming from H and Z decays. A brief discussion concerning the case $M_H \not\approx M_Z$ is also given.

[1]E-mails: Moretti@to.infn.it; Moretti@hep.phy.cam.ac.uk.

1. Introduction

If the Standard Model ($\mathcal{SM}$) Higgs boson has a mass around 90 GeV, it is degenerate with the neutral electroweak (EW) boson Z ($M_Z \approx 91.175$ GeV). Although the model itself does not show any preference for this value, such a condition could well occur in nature. At this mass the Higgs particle predominantly decays into $b\bar{b}$–pairs, and this is also a possible signature of the Z–vector. Therefore, whenever the two bosons are contemporaneously produced, their peaks overlap in the invariant mass spectrum of the decay products and cannot be separated, not even for optimistic detector performances[2]. However, a closer inspection of the candidate $b\bar{b}$–sample (in a window around $M_H \approx M_Z$) should reveal a b–quark content larger than the one arising from Z–decays only. This would then allow one to recognise the presence of the Higgs boson. To this end, the fact that the Higgs Branching Ratio (BR) into b–quarks is $\approx 90\%$ (for $M_H \approx 90$ GeV), whereas $Z \to b\bar{b}$ constitutes only 22% of the possible hadronic Z–decays, is very helpful[3].

A Higgs boson with $M_H \approx M_Z$ was beyond the discovery potential of LEP I. Unless the Tevatron is able to detected it in the short term, the first machine where such a particle can be searched for is LEP II, provided that its Centre–of–Mass (CM) energy reaches ≈ 200 GeV. In fact, at this energy, the machine will be beyond the threshold of an on–shell ZH–pair, which is the dominant Higgs production mechanism at LEP II. Recently, it has been assessed [1] that the cleanest Higgs signature at LEP II is the one proceeding through the decays $Z \to \mu^+\mu^-$ and $H \to b\bar{b}$ (the 'golden channel'), although also other final states can be considered ($H \to \tau^+\tau^-$ and $Z \to e^+e^-, \nu\bar{\nu}$, jets). In the more distant future, high precision Higgs physics can be performed at the Next Linear Collider (NLC, with $\sqrt{s} = 350 - 500$ GeV) [2]. An e^+e^- linear machine has a clear advantage with respect to hadron colliders. Because of the reduced QCD background at the former, one can more easily exploit the $H \to b\bar{b}$ decay channel, whereas at the latter extremely high b–tagging efficiency and not–b–jet rejection are required in order to make Higgs detection feasible[4].

At LEP II the case $M_H \approx 90$ GeV will require the highest CM energy option, which

[2] In fact, the Higgs width Γ_H, for $M_H = 90$ GeV, is ≈ 2.4 MeV, whereas experimental resolutions are generally comparable or larger than the Z width, $\Gamma_Z = 2.5$ GeV.

[3] An experimental method of discriminating between jets that originate from b–quarks and those produced by light quarks and gluons, namely b–tagging, has been successfully exploited in the past few years, especially at LEP I and the Tevatron. The method requires one to tag hadronic events with secondary vertices.

[4] At the moment, it is not clear whether this will be possible or not, particularly in case of Z–H mass degeneracy. For discussions about the Higgs discovery potential of future hadronic machines, see Refs. [3, 4].

corresponds to a second stage of the project of the machine, therefore quite far in the future. Furthermore, by assuming an yearly luminosity of 500 pb^{-1} for the CERN collider and of 20 fb^{-1} for the linear machine, one ends up with a number of events that is larger in the second case. Also, whereas the gauge and Higgs bosons produced at LEP II would be practically at rest, such that their decay products are generally soft and uniformly distributed over the accessible phase space, at NLC energies these have a strong boost, making their tagging relatively easier. For all these reasons we believe that the NLC will still play a decisive rôle in detecting and, particularly, in studying the properties of a Higgs boson with a mass near M_Z.

We earlier mentioned that the ZH–channel is the largest Higgs production mechanism at LEP II. If $M_H \approx M_Z$, at $\sqrt{s} \approx 350$ GeV it is still the dominant process, whereas at $\sqrt{s} \approx$ 500 WW–fusion has bigger rates (ZZ–fusion is smaller than $e^+e^- \to ZH$) [5]. However, the ZH–mechanism has a few advantages with respect to the WW–one: its final state is fully constrained and it allows Higgs spin, parity and branching ratio determinations (see [6, 7] and references therein). Thus, the ZH–process is of a crucial importance even in energy regimes where it is not the largest Higgs production mechanism. This is the reason why we concentrate here on the bremsstrahlung process only. In addition, we restrict our attention to the case $H \to b\bar{b}$ (as the corresponding BR is much larger than that one into taus). Concerning the Z–boson, we select muon decays only, thus avoiding complications due to hadronic final states (when Z goes into jets or taus), to additional t–channel backgrounds (for $Z \to e^+e^-$) and to the loss of kinematical constraints (final state neutrino).

The story of theoretical studies of the process $e^+e^- \to ZH$ dates back to Refs. [8, 9, 10], where the Born cross section was first computed. In Ref. [11] the leading order (LO) cross section for $e^+e^- \to f\bar{f}H$ was calculated analytically. Next–to–leading order (NLO) EW corrections were computed later [12, 13, 14, 15, 16, 17][5]. As for $M_H \approx 90$ GeV the Higgs width Γ_H is a few MeV only, the Higgs boson can be safely kept on–shell in the computations. However, for phenomenological studies, the full final state, including the Higgs decay products, has to be known. Therefore, signal and background processes of the type, e.g., $e^+e^- \to \mu^+\mu^- b\bar{b}$, must be considered. Recently, tree–level semi–analytical cross sections for $e^+e^- \to \mu^+\mu^- b\bar{b}$ events were given [18, 19, 20]. Alternatively, one can exploit a Monte Carlo [6, 21] or a 'deterministic' approach [22].

It is the purpose of this paper to quantify the influence on the cross section of hard

[5]For a review, see [14] (and references therein).

photon emission, which can take place in the process $e^+e^- \rightarrow \mu^+\mu^- b\bar{b}$. In fact, contrary to LEP I, where the Z–resonance imposes a natural cut–off on events with hard photons produced by the initial state, at LEP II and NLC such a suppression does not act any longer and, in addition, as the beam energy is larger, the probability that the incoming electrons and positrons can radiate increases. It follows that a sample of pure $e^+e^- \rightarrow \mu^+\mu^- b\bar{b}$ events, without γ–radiation, does not exist in practise and one has to deal inevitably with electromagnetic (`e.m.`) emission. We also notice how all particles in the final state are *charged* and therefore can also radiate hard photons.

The inclusion of higher order `e.m.` effects is especially important in the case $M_H \approx M_Z$, since radiative corrections modify the relative content of H– and Z–decays in the candidate $b\bar{b}$–sample. This is true whether one adopts missing mass techniques by computing the invariant mass recoiling against the tagged $\mu^+\mu^-$–pair, or one attempts the reconstruction of the $b\bar{b}$–signal directly from the b–jets [23]. In the first case, photons enter in the M_{recoil} spectrum and also spoil the reconstruction of the Z–boson via the tagged muons, since these latter can emit `e.m.` radiation after the Z–decay. In the second case, as γ–radiation can take place also off b–quark lines in the Higgs decay process, such effects are equally present (although with a reduced probability since $|Q_b| = 1/3 < |Q_{e,\mu}| = 1$ and because only half of the diagrams occurring in case of radiation from leptons are involved here). To avoid this, one could try to include photons by looking at the $M_{b\bar{b}\gamma}$ invariant mass. But such a procedure would also be distorted by unwanted γ–radiation produced by e^+e^- and $\mu^+\mu^-$ pairs. Moreover, the knowledge of the absolute size of the corrections for real photon emission could help if one discriminates between a $\mathcal{SM}$ Higgs boson and a possible neutral scalar from Supersymmetric models, and/or in testing the Yukawa coupling of the Higgs particle.

In general, the hard `e.m.` radiation affects the kinematics of the $\mu^+\mu^- b\bar{b}$ events in various ways. First, the presence of a hard photon modifies the two–body decay kinematics of the process $e^+e^- \rightarrow ZH \rightarrow \mu^+\mu^- b\bar{b}$ [24, 25], as photon emission cannot be unambiguously assigned to one or the other of its three possible sources: e^+e^-, $\mu^+\mu^-$ and $b\bar{b}$. Second, the radiated photon will affect a cut around M_Z on the $\mu^+\mu^-$–pair, which allows one to get rid of a large part of the backgrounds in the non–radiative case. In fact, many of the configurations coming from the ZH signal do have muons whose invariant mass does not peak at the Z–pole. In this respect, as the radiation from the e–lines is concentrated to a large extent along the beam direction and that from b–quark lines is suppressed by the charge Q_b, as a consequence, the μ–lines are the main source of detected photons. Finally, the number of background diagrams leading to $\mu^+\mu^- b\bar{b}\gamma$ final states in e^+e^- initiated processes is very large (168 Feynman graphs at tree–level, neglecting 62 diagrams which include a suppressed $H\mu\mu$ Yukawa coupling), compared to the number of those involving the Higgs resonance (6 graphs at tree–level)[6].

In carrying out our analysis, we will make some simplifications, which should not modify the conclusions we will get in the end. We will perform only a tree–level calculation of the processes $e^+e^- \to \mu^+\mu^- b\bar{b}$ and $e^+e^- \to \mu^+\mu^- b\bar{b}\gamma$ (with the photon emitted both from the initial and the final state). We will however 'dress' the former with the Initial State Radiation (ISR) [26], implementing this latter by means of a convolution with electron structure functions [27] (in particular, we use the expressions given in Ref. [28])[7]. This is done in order to be able to sum up the rates corresponding to the two above processes, through the order $\mathcal{O}(\alpha_{em}^5)$. In fact, the ISR formulae, as given in Ref. [28], include the exact photon corrections to the e^+e^- annihilation subprocess up to the second order in the `e.m.` coupling constant (in particular, they also embody hard photon emission). For consistency, we implemented only $\mathcal{O}(\alpha_{em})$ ISR terms (the inclusion of the $\mathcal{O}(\alpha_{em}^2)$ pieces does not change significantly the size of such corrections). By computing the total cross section of the leading $(2 \to 4)$ reaction supplemented by the ISR and that one of the radiative $(2 \to 5)$ process, we are then able to separate at the order α_{em}^5 the contribution due to hard photon emission from the one due to collinear and soft `e.m.` radiation (see below the cut in transverse momentum) and to virtual corrections. In particular, we combine the two approaches by subtracting the radiative $(2 \to 5)$ Matrix Element (ME) from the leading log $\mathcal{O}(\alpha_{em})$ part of the ISR, to avoid double counting (see also Ref. [29, 30]). In the following, the label 'LO' will identify rates obtained from the $2 \to 4$ process dressed with ISR and with the hard emission subtracted, whereas 'NLO' will refer to rates obtained from the $2 \to 5$ reaction involving hard `e.m.` radiation only. This subtraction is performed between, on the one hand, the graphs in Fig. 1 and, on the other hand, those in Figs. 2–4 in which photons are connected to electron and positron lines: i.e., 1 & 2 in Fig. 2, 1–2, 7–9 & 14 in Fig. 3, 1–2 & 8–9 in Fig. 4. Since in neutral current processes ISR and Final State Radiation (FSR) are separately gauge invariant, this procedure is legitimate here.

The above procedure is adopted for the case of the dominant, universal, factorisable and process independent contribution to the complete set of ISR corrections to four–fermion

[6]At leading order in $e^+e^- \to \mu^+\mu^- b\bar{b}$ events one has 24 and 1 diagrams, respectively, again excluding 9 diagrams with $H\mu\mu$ couplings.

[7]We neglect to consider Linac energy spread and beamsstrahlung, as they are negligible compared to the ISR, at least for the 'narrow' D-D and TESLA collider designs [26]. These effects would however be straightforward to insert.

production, containing all mass singularities $L = \ln(s/m_e^2)$ and expressed via the ISR 'radiator', as known from s–channel e^+e^- annihilations[8]. In addition to these, there are also non–universal, non–factorisable and process dependent ISR corrections, which arise in association with t– and u–channel electron exchanges (neutrino, in case of charged currents). The full set of formulae needed to incorporate the complete ISR in `CC3, NC2 and NC8` [31] $e^+e^- \to 4$ fermion processes has been recently given, in Ref. [32]. Whereas Higgs signals (graph d in Fig. 1) and non resonant background contributions (graphs b and c in Fig. 1) proceed via s–channel annihilations, the remaining background contributions (graphs a in Fig. 1) do through t– and u–electron channels, involving ZZ–, $Z\gamma$– and $\gamma\gamma$–production (i.e., `NC8`–type diagrams). Thus, we could well apply non–universal ISR corrections to these latter contributions. However, it has been shown in Ref. [32] that they are generally smaller by an order of magnitude with respect to the universal ones. Furthermore, one has to consider that we are concerned with Higgs searches for $M_H \approx M_Z$, such that in the end (after the Higgs selection procedure) the dominant background is ZZ–production (i.e., `NC2`–type graphs), for which the non–universal ISR corrections are even more suppressed. For these reason then, we neglect here such effects.

Compared to the universal ISR, QED corrections related to the final state (FSR) are much smaller (and comparable to the non–universal ISR corrections [29, 32, 33, 34]). Typical suppressions of the order $\mathcal{O}(\Gamma/M)$ are expected for the interferences between ISR and FSR in resonant boson pair production as well as in inter–bosonic final state interferences [35]. We do not expect these effects to be relevant for Higgs production either. Thus, because of their small size, we do not include them in our analysis.

We also ignore genuine weak corrections, as these have been proved to be well under control (at least for the on–shell process $e^+e^- \to ZH$) [36].

We further stress that, on the one hand, a calculation including even part of the above effects would be extremely CPU–time consuming, because of the large number of Feynman diagrams involved in the processes studied, which have up to seven external particles and multiple Breit–Wigner resonances in different regions of phase space. On the other hand, a full $\mathcal{O}(\alpha_{em}^5)$ calculation is well beyond the intentions of this paper.

A further simplification we have adopted is to avoid computing some of the interference terms of the two processes $e^+e^- \to \mu^+\mu^- b\bar{b}(\gamma)$, which either vanish identically or are extremely small compared to the squared terms of the MEs. Finally, we do not discuss the QCD background, $e^+e^- \to Z + n$ jets (with $n \geq 2$), as this is largely suppressed if all

[8]Naively, ISR universal effects tend to reduce the effective beam energy, thus modifying both the normalisation and the shape of the differential distributions which are of interest in Higgs searches.

jets are well separated (as we assume throughout this paper) and they have to reproduce the Higgs mass, $M_{\rm jets} \approx M_H$.

Finite width effects for the Z and H are included[9]. The masses of both b–quarks and muons are non–zero, apart from the case of the $H\mu\mu$ coupling, in which m_μ has been set equal to zero, thus eliminating the corresponding diagrams from the MEs. No effort has been made to simulate experimental effects, in particular in detecting b–quarks, apart from assigning plausible values for the b–tagging efficiency ϵ_b and the misidentification probability $\epsilon_c{}'$ of c as a b. We cut on the transverse momentum (with respect to the beam direction) of each particle in the final state, $p_T^{all} > 1$ GeV, which, on the one hand, is reasonably compatible with detector requirements and, on the other hand, protects our radiative MEs from both divergences and numerical instabilities. Hence, this value of transverse momentum also defines the phase space region of soft and collinear photons (i.e., $p_T^\gamma < 1$) emitted from the incoming e^+e^-–lines where we make use of the ISR (as described above).

In the next Section we give an account of the numerical calculations; in Section 3 we present and discuss our results and Section 4 gives our conclusions.

2. Calculation

For $M_H \approx M_Z$, both at LEP II and at the NLC the cleanest Higgs signature in the intermediate mass range will be via the process

$$e^+e^- \to \mu^+\mu^- b\bar{b}. \tag{1}$$

The corresponding Feynman diagrams for background (graphs a, b and c) and signal (graph d) contributions are depicted in Fig. 1[10]. Among the background graphs, one distinguishes between 'conversion diagrams' (Fig. 1a) and 'annihilation diagrams' (Fig. 1b,c). They are also called `crab` and `deer` diagrams, respectively, further dividing these latter into μ–`deer` (Fig. 1b) and b–`deer` (Fig. 1c) diagrams [18, 19, 20]. By inserting the appropriate type of internal propagator (γ or Z) and by performing all the possible permutations of the boson lines on the fermion ones one can get out of the background diagrams of Figs. 1a–c a total of 24 diagrams, 8 per each kind of graphs (a, b and c). The signal diagram in Fig. 1d is unique.

[9]We are not concerned about possible gauge invariance violations due to bremsstrahlung off unstable particles, as there is no cancellation here which could amplify such effects.

[10]Here and in the following we adopt the labelling: e^+ (1), e^- (2), μ^+ (3), μ^- (4), b (5), $\bar{b}$ (6) and γ (7).

To obtain the Feynman graphs representative of the radiative process

$$e^+e^- \to \mu^+\mu^- b\bar{b}\gamma, \tag{2}$$

one has to add a real photon in all possible ways to the diagrams of Fig. 1. This is a topologically trivial matter, however, the total number of graphs to be computed is very large. The case of the signal is the simplest, as one obtains the 6 diagrams of Fig. 2 (here the wavy internal lines represent a Z). For the case of the `crabs` one gets 56 diagrams in total, as indicated by Fig. 3 (in which an internal wavy line represents both a γ and a Z). This is also the number that one gets from the `deers` (both for μ and b, see Fig. 4). In total, one ends up with 174 diagrams at tree–level. As already mentioned, we did not consider 62 diagrams involving $H\mu\mu$ Yukawa couplings.

More than from the large number of graphs, complications in computing the cross section for process (2) arise from the fact that they have in general rather different resonant structures over the accessible phase space. For example (see Fig. 2), the signal diagrams present Breit–Wigner peaks of the type $H \to b\bar{b}$, $H \to b\bar{b}\gamma$, $Z \to \mu\bar{\mu}$ and $Z \to \mu\bar{\mu}\gamma$. For the backgrounds, in addition to the two already mentioned Z–resonances, one also finds $Z \to b\bar{b}$ and $Z \to b\bar{b}\gamma$ peaks, together with diagrams which are not resonant at all (for example, the ones in Fig. 3 when all the internal wavy lines are identified with virtual photons)[11]. The (numerical) integration must carefully take into account this diversified structure.

We computed the cross sections by using the packages MadGraph [37] and HELAS [38] for the Feynman diagram evaluation and VEGAS [39] for the integration over the phase space. For VEGAS, we split the total Feynman amplitude squared into a sum of non–gauge–invariant terms (as already done in Refs. [25, 40]), each of which has a particular resonant structure, and integrate them by using appropriate phase spaces which absorb the Breit–Wigner peaks in the integrand. In general, the change of variable

$$Q^2 - M^2 = M\Gamma\tan\theta, \longrightarrow dQ^2 = \frac{(Q^2-M^2)^2 + M^2\Gamma^2}{M\Gamma}d\theta, \tag{3}$$

where Q, M, Γ stand for the virtuality, the mass and the width of the resonance, gives an integrand which depends smoothly on θ. For example, in Fig. 2, it is convenient to isolate three terms, i.e., the amplitude squared of the graphs: i) 1 & 2; ii) 3 & 4; iii) 5 &

[11]As we will be eventually interested in studying the distributions in the invariant masses $M_{b\bar{b}}$ and $M_{b\bar{b}\gamma}$, for the time being we do not discuss here the fact that also resonances of the type $Z \to \mu^+\mu^- b\bar{b}$ can appear in the case of the `deers`, see, e.g., graph 1 of Fig. 4 (in which the wavy line attached to the incoming fermions represents a Z and the one joining μ– and b–lines is a photon).

6, and to compute them separately by means of different phase spaces. The interferences between the set of diagrams in i), ii) and iii) are the last contribution to the part of the total ME which includes Higgs resonant graphs. In a similar way, one proceeds with the background graphs in Figs. 3–4.

Such a procedure gives a substantial reduction of the integration errors, although some diagrams need to be computed twice or more (e.g., diagrams 1 & 2 in Fig. 2 are necessary for the $|M_1 + M_2|^2$ term as well as for some of the interferences). This apparently increases the final CPU time of the run. However, the competition between these two aspects (i.e., high precision but multiple Feynman diagram evaluations) is such that the computing time needed to get a given accuracy is much less than that required to integrate the differential cross section without any special care, especially when one uses adaptive algorithms for the multi–dimensional integrations, as we have here.

Among the different non–gauge–invariant terms one has to deal with, the interferences between the various sets (of signal, `crabs`, μ– and b–`deers`) as well as the ones between graphs within the same set are the most complicated, as these generally mix up graphs with different resonant structures[12]. However, this often implies that they are small compared to the amplitudes squared of diagrams with identical composition of Breit–Wigner peaks, since the phase space region in which one or more graphs are large is different. Therefore, a useful and time–saving procedure is to neglect such terms, whenever possible.

For example, concerning the leading order process (1), it has been shown in Ref. [20] that the various Higgs–background interferences either vanish identically or are small, so that they can be safely neglected. In the case of the interferences between the various sources of background such a suppression is less visible [18]. We have checked whether this remains true in presence of hard photon radiation. For example, by interfering the signal diagrams of Fig. 2 with the `crabs` and `deers` of Figs. 3 and 4 together, one obtains mixed terms which are negligible compared to all the squared contributions, whereas mixing the various sets of `crab` and `deer` diagrams of Figs. 3 and 4 yields interferences which are of the same order as some of the amplitudes squared. This also happens for the interferences within the sets of Figs. 2, 3 and 4, if treated separately: that is, when one splits the modulus squared of the signal process represented in Fig. 2 as previously described, and those of the backgrounds in Figs. 3 and 4 by isolating the Z–resonances out of the graphs with γ–propagators. In this respect, we found it useful to recognise within the `crab` diagrams of Fig. 3 the components with the following resonant structures: i) $Z \to \mu^+\mu^-(\gamma)$ and

[12]We have integrated them by using a flat phase space, which does not map any of the possible peaks of the interfering graphs.

$Z \to b\bar{b}(\gamma)$; ii) $Z \to \mu^+\mu^-(\gamma)$ and $\gamma \to b\bar{b}(\gamma)$; iii) $\gamma \to \mu^+\mu^-(\gamma)$ and $Z \to b\bar{b}(\gamma)$; iv) $\gamma \to \mu^+\mu^-(\gamma)$ and $\gamma \to b\bar{b}(\gamma)$. In the following, we will refer to them as ZZ, $Z\gamma$, γZ and $\gamma\gamma$ backgrounds. A Z–resonance is present also in the diagrams of Fig. 4, however, we will refer to these collectively as μ– and b–`deers` (although in the computations their resonant structure has been appropriately taken into account), as these diagrams are very suppressed if compared to those in Fig. 3 and also because they do not have the two–to–two and two–to–three kinematics typical of the signal (compare to Fig. 2). As already stressed, we recall here that all these amplitude contributions we have been discussing must be summed up together in the end. However, if taken separately, they provide a useful way of looking inside the process and distinguishing between the different fundamental interactions. In summary, in the results we will present in the next section, we have systematically neglected interferences between the signal and the backgrounds whereas we have kept all the others.

The following numerical values of the parameters have been adopted: $M_Z = 91.175$ GeV, $\Gamma_Z = 2.5$ GeV, $M_W = 80.23$ GeV, $\Gamma_W = 2.2$ GeV, and for the Weinberg angle we have used its leptonic effective value of $\sin^2_{\rm eff}(\theta_W) = 0.2320$. For the fermions: $m_\mu = 0.105$ GeV and $m_b = 4.25$ GeV. The `e.m.` coupling constant α_{em} has been set equal to 1/128. For the Higgs width Γ_H we have adopted the tree–level expression corrected for the running of the quark masses in the vertices $Hq\bar{q}$ (these have been evaluated at the scale $\mu = M_H$ [41]). Therefore, in order to be consistent, we have used a running b–mass in the $Hb\bar{b}$ vertex of the production process here considered. As representative values of the CM energy of LEP II and NLC we have adopted 200, and 350, 500 GeV, respectively, whereas the Higgs mass has been fixed at 90 GeV.

3. Results

In the non–radiative process $e^+e^- \to \mu^+\mu^- b\bar{b}$ Higgs signals should appear as narrow resonances in the invariant mass spectrum of the Higgs decay products over the contribution due to the background processes, which are generally flat, apart from the region around M_Z, where the Z peak (due to the ZZ `crab` diagrams of Fig. 1a) clearly sticks out. In order to detect Higgs signals via the two–b–two–μ channel one can adopt two different strategies [23][13]:

[13]We ignore the full reconstruction of the reaction $e^+e^- \to ZH$ via the decays into jets and/or leptons of both the H– and the Z–boson, by fitting their kinematics, because it would present additional complications, which are beyond the intentions of this study [23].

- the calculation of the missing mass recoiling against the reconstructed $Z \to \mu^+\mu^-$, by plotting the distribution in $M_{recoil} = \sqrt{[(p_{e^+} + p_{e^-}) - (p_{\mu^+} + p_{\mu^-})]^2}$ and exploiting tagging on the $\mu^+\mu^-$–system only;
- direct reconstruction of the H–peak from the b–jets, by plotting the distribution in $M_{b\bar{b}} = \sqrt{(p_b + p_{\bar{b}})^2}$.

Once a hard photon is included via the process $e^+e^- \to \mu^+\mu^- b\bar{b}\gamma$, the next–to–leading order contribution to the first spectrum coincides with the invariant mass of the $b\bar{b}\gamma$–system, thus the rates up to the order α_{em}^5 in the recoiling mass are the sum of the distributions $M_{b\bar{b}}$ at LO and $M_{b\bar{b}\gamma}$ at NLO. In the second approach, the full rates up to α_{em}^5 in the $M_{b\bar{b}}$ spectrum are given by the sum of the $b\bar{b}$–invariant masses at leading and next–to–leading order. We expect the possible alternative strategy we outlined in the Introduction (i.e., to look at the 'pure' $M_{b\bar{b}\gamma}$ spectrum) to be less successful, because in this case one would be able to correctly reconstruct Higgs peaks only in the case of diagrams 5 and 6 (of Fig. 2), which give a suppressed contribution to the total $e^+e^- \to \mu^+\mu^- b\bar{b}\gamma$ cross section. In presenting our results, we concentrate then on the two spectra $M_{b\bar{b}}$ and $M_{b\bar{b}\gamma}$, with $M_H \approx M_Z$.

In order to suppress the backgrounds γZ and $\gamma\gamma$ (among the `crabs`) as well as the contributions from the μ– and b–`deers`, we require that the invariant mass of the muon pair reproduces a Z–boson, by applying the cut, e.g., $\Delta M_Z \equiv |M_{\mu^+\mu^-} - M_Z| < 10$ GeV [6, 23]. In this way, we mainly select the ZZ contribution from the `crabs`, since the $Z\gamma$ one will be largely suppressed in the end by a cut around M_H. In this way, one is able to compare $Z \to b\bar{b}$ and $H \to b\bar{b}$ decays [23]. Furthermore, in order to reduce the content of Z–decays in the candidate $b\bar{b}$–sample we consider events for which $|\cos\theta_{\mu^+\mu^-}| < 0.8$ [23] (where $\theta_{\mu^+\mu^-}$ is the angle of the reconstructed Z–boson with respect to the beam), since $e^+e^- \to ZZ$ events are strongly peaked in the forward/backward direction due to the t,u–channel exchange of electrons [42][14].

Tables I–III show the cross sections in a window of 20 GeV, centered around $M_H = 90$ GeV (i.e., we consider events with $\Delta M_H \equiv |M_{b\bar{b}(\gamma)} - M_H| < 10$ GeV), for the signals $e^+e^- \to ZH \to \mu^+\mu^- b\bar{b}(\gamma)$ (S, the square of the last diagram in Fig. 1 at LO and of those in Fig. 2 at NLO) and the total backgrounds $e^+e^- \not\to ZH \to \mu^+\mu^- b\bar{b}(\gamma)$ (B, the square of the sum of the first three sets of graphs in Fig. 2 at LO and of those in Figs. 3 and 4 at NLO), together with the total significance Σ, for the integrated luminosity $\mathcal{L} \equiv \int Ldt = 0.5(20)$ fb^{-1} *per annum* at LEP II(NLC), for $\sqrt{s} = 200$ (Table I), 350 (Table II) and 500 GeV

[14]This is also true for the cases $Z\gamma$, γZ and $\gamma\gamma$.

(Table III). All the mentioned constraints have been applied: that is, $p_T^{\mu,b} > 1$ GeV, $\Delta M_Z < 10$ GeV and $|\cos\theta_{\mu^+\mu^-}| < 0.8$. In case of cross sections (S and B columns), the label NLO identifies rates from the radiative process $e^+e^- \to \mu^+\mu^- b\bar{b}\gamma$ only (with $p_T^\gamma > 1$ GeV). In particular, the second line represents rates obtained from the distribution in invariant mass of the system $b\bar{b}\gamma$, whereas the other refers to rates obtained from the $M_{b\bar{b}}$ spectrum. In case of significances (Σ columns), the label NLO give rates obtained through the order $\mathcal{O}(\alpha_{em}^5)$ (all photons) in case of the direct reconstruction method (upper line) and of the missing mass analysis (lower line), as obtained by adopting the subtraction procedure described in the Introduction. According to this treatment, LO refers here to rates from the process $e^+e^- \to \mu^+\mu^- b\bar{b}$ corrected for universal ISR effects due to virtual and real photons (these latter with $p_T^\gamma < 1$ GeV). For reference, we also give (in square brackets) cross sections and significances when no radiation is present, as obtained by integrating the spectra in Fig. 5.

In computing the Σ's (see Ref. [6]), we neglect the (small) probability of misidentification of light quarks and gluons as b's and we assume $BR(H \to b\bar{b}) >> BR(H \to c\bar{c})$. Then, the probability of picking one b out of two is $[1-(1-\epsilon_b)^2]$, whereas the total significance Σ is

$$\Sigma = \sqrt{\mathcal{L}}\ \frac{\sigma(e^+e^- \to ZH \to \mu^+\mu^- b\bar{b}(\gamma))}{\sqrt{\sigma(e^+e^- \not\to ZH \to \mu^+\mu^- b\bar{b}(\gamma))}} P_b, \tag{4}$$

with

$$P_b = \frac{1-(1-\epsilon_b)^2}{\sqrt{[1-(1-\epsilon_b)^2] + \delta[1-(1-\epsilon_c{}')^2]}}, \tag{5}$$

where the factor δ has been introduced in order to remind the reader that the EW couplings $\gamma^*, Z \to q\bar{q}(\gamma)$ are generally different, depending whether $q = c$ or b. However, to use $\delta = 1$ in formula (4) is always a good approximation for our analysis. In fact, on the one hand, the background B practically coincides at tree–level with the ZZ–piece and $BR(Z \to b\bar{b}) \approx BR(Z \to c\bar{c})$. Whereas, on the other hand, the NLO rates (for which $BR(Z \to b\bar{b}\gamma) \approx 1/4\ BR(Z \to c\bar{c}\gamma)$, although this does not occur in all diagrams) have to be added to the LO ones to produce the correct significances, such that the effect of the different `e.m.` coupling is largely washed out in the end[15]. We consider the following five combinations of b–tagging efficiency (ϵ_b) and $c \to b$ misidentification ($\epsilon_c{}'$): $\epsilon_b = 1$ and $\epsilon_c{}' = 0$ (perfect tagging), and $\epsilon_c{}' = 0.2\epsilon_b$ [23], for $\epsilon_b = 0.2, 0.4, 0.6, 0.8$.

[15]The value of δ would be different from 1 when using the NLO rates on their own, but Σ's computed in this way have no meaning for the present analysis.

Before proceeding further, a few points concerning the background due to top events are worth mentioning here. In fact, $t\bar{t}$–production followed by the decay $t\bar{t} \to b\bar{b}\mu^+\mu^-(\gamma)X$ gives the same signatures as the signal processes (both at leading and next–to–leading order, with X representing missing particles). As m_t should be around or greater than 175 GeV [43, 44], top–antitop production will not take place at LEP II. On the contrary, at the NLC, $t\bar{t}$–pairs will be copiously produced: the study of the top properties (especially around the threshold) is, in fact, one of the main physics goals of this machine. In order to quantify at leading order the importance of $e^+e^- \to t\bar{t}$ events (we do not consider non–top and single top–diagrams, as, for the purposes of this study, they can be safely neglected [45])[16], we have run the code used in Refs. [25, 45], for the choice of CM energies adopted here, with the decays $W^+ \to \mu^+\nu_\mu$ and $W^- \to \mu^-\bar{\nu}_\mu$. In order to have a realistic estimate of the cross section at threshold for $t\bar{t}$–events at a $\sqrt{s} = 350$ GeV NLC, we have taken $m_t = 174$ GeV for the top mass (see Ref. [47], where differences $\sqrt{s} - 2m_t \approx 2$ GeV were also considered). As we are interested in $t\bar{t} \to b\bar{b}W^+W^-$ events faking possible Higgs signals in the $b\bar{b}$–channel, we look at the rates in the $2\Delta M_H$ window. We also apply the cuts in ΔM_Z, $\cos\theta_{\mu^+\mu^-}$ and $p_T^{\mu,b}$. Because of the relatively small BR of the charged vector bosons into muons (in fact, $BR(W^- \to \mu^-\bar{\nu}_\mu) \approx 11\%$), the rates for $b\bar{b}W^+W^-$ events with $M_{b\bar{b}}$ around $M_H = 90$ GeV are rather small. For the non–radiative process one finds about 2×10^{-2} and 9×10^{-2} fb, at $\sqrt{s} = 350$ and 500 GeV, respectively. In presence of real hard photon radiation[17], rates are even more suppressed compared to the signal ones: they are of the order 10^{-4} and 10^{-3} fb, respectively. In addition, $t\bar{t}$–events have a quite large value of missing energy, i.e., $E_{miss} \gtrsim 35 - 40$ GeV (because of the neutrinos from the W–decays, which escape the detectors), whereas the final states $\mu^+\mu^-b\bar{b}(\gamma)$ are in principle fully constrained: this should eventually allow a further reduction in the importance of top events. Therefore, we can neglect them in the present analysis.

By looking at Tables I–III it is clear how the knowledge of the rates due to process (2) with a hard photon can be important in successfully carrying out a b–tagging analysis, especially at NLC energies and if one adopts the direct reconstruction method. In fact, the signal and background LO rates obtained in the window $\Delta M_H < 10$ GeV are generally

[16]We also neglect QCD (and QED) Coulomb–like interactions between the two top quarks at threshold [46]. Both because the large top mass implies that the typical spikes at $\sqrt{s} \approx 2m_t$ do not show dramatically up in the excitation curve and also because their inclusion would not change our conclusions about the importance of the $t\bar{t}$–background.

[17]For the process $e^+e^- \to t\bar{t} \to b\bar{b}\mu^+\mu^-\gamma X$ we have used a `FORTRAN` code produced by MadGraph and HELAS interfaced with routines generating the $W^+ \to \mu^+\nu_\mu(\gamma)$ and $W^- \to \mu^-\bar{\nu}_\mu(\gamma)$ decays (again, only the $t\bar{t}$–resonant graphs have been considered).

of the same order as the corrections that one gets from the $M_{b\bar{b}}$ NLO spectra, whereas the rates obtained from the $M_{b\bar{b}\gamma}$ distributions are negligible compared to those from $M_{b\bar{b}}$ at LO. The NLO corrections are relatively larger at $\sqrt{s} \gtrsim 350$ GeV than at $\sqrt{s} \approx 200$ GeV. The overall effect is a relative increase of the background component in the $b\bar{b}$ candidate sample, although only of a few percent (at all values of $\sqrt{s}$). The cross sections in Tables I–III also show how an analysis that considers only radiative events $e^+e^- \to \mu^+\mu^- b\bar{b}\gamma$ with $p_T^\gamma > 1$ GeV and uses exclusively the spectrum in $M_{b\bar{b}\gamma}$ would be more complicated, as rates are at least one order of magnitude smaller than those obtained from the sum of LO and NLO cross sections, and because the relative excess of signal events is reduced. Furthermore, for the $M_{b\bar{b}\gamma}$ rates separately, significances would be much smaller (see also Figs. 6–8).

Figs. 5a–c shows the differential distribution in $M_{b\bar{b}}$ for the non–radiative process $e^+e^- \to \mu^+\mu^- b\bar{b}$[18], for the signal (shaded) and the total background. The same sequence of cuts as in the Tables has been implemented here (apart from the restriction in the window $M_{b\bar{b}} \approx M_H$). Rates are shown for $\sqrt{s} = 200$ (Fig. 5a), 350 (Fig. 5b) and 500 GeV (Fig. 5c), with $M_H = 90$ GeV, plotting the histograms by bins of 2 GeV. In Fig. 6–8 we present the spectrum in $M_{b\bar{b}}$ (a) and in $M_{b\bar{b}\gamma}$ (b) in the case of the radiative process $e^+e^- \to \mu^+\mu^- b\bar{b}\gamma$ (with $p_T^\gamma > 1$ GeV), for the signal (shaded), and the total background. The combination of $\sqrt{s}$ and M_H is the same as in the previous three plots.

The interpretation of Figs. 5a–c is quite straightforward: the signal clearly shows a narrow peak at $M_H = 90$ GeV, whereas the background (which includes the sum of the all contributions from `crabs` and `deers` of Fig. 1) has a broader structure. The ZZ component contributes with the typical $Z \to b\bar{b}$ peak, whereas the tail at small values of $M_{b\bar{b}}$ is largely due to $Z\gamma$ background events. The steep fall of $M_{b\bar{b}}$ around 120 GeV at $\sqrt{s} = 200$ GeV is a kinematical effect due to the limited CM energy available at LEP II, whereas the long tail for $M_{b\bar{b}} > 90$ GeV at the NLC is an effect due to ZZ (and also γZ) events. The $\gamma\gamma$–term as well as the `deers` and the various interferences are smaller and do not bring any substantial feature into the total spectrum. In general, `deers` are bigger than the $\gamma\gamma$ `crabs`, and b–`deers` dominate over μ–ones, especially at higher energies, whereas the total interference (of the background) is at the same level as the b–`deers`. As already mentioned, the interference between signal and background is negligible with respect to

[18]That is, the $2 \to 4$ process, without any ISR effect. When `e.m.` emission from the incoming e^+e^-–lines is included (with $p_T^\gamma < 1$ GeV), shapes and normalisations are generally different. However, we have not plotted here the corresponding curves, since in order to obtain them in the region of interest (i.e., $\Delta M_H < 10$ GeV) it is enough to renormalise those in Fig. 5, according to the rates given in Tables I–III.

the terms discussed above and, for simplicity, it has not been included into the figures.

The presence of a hard photon ($p_T^\gamma > 1$ GeV) significantly modifies the lowest order distributions in the $b\bar{b}$–invariant mass (especially of the Higgs process), see Figs. 6–8. By looking at the $M_{b\bar{b}}$ spectrum in the case of the signal one easily recognises the tail at small invariant masses due to the $b\gamma$–component, whereas the $e\gamma$– and $\mu\gamma$–diagrams contribute to the resonance around 90 GeV. In the case of the spectrum in $M_{b\bar{b}\gamma}$ it is the other way round. Here, the Breit–Wigner peak comes from the amplitude squared due to graphs 5 & 6 in Fig. 2, whereas diagrams 1 & 2 and 3 & 4 appear via the tail at values of $M_{b\bar{b}\gamma}$ greater than 90 GeV. Although not plotted in the figures, we note that the contributions from the $\mu\gamma$ diagrams are comparable to those from the $e\gamma$ ones at LEP II, whereas at NLC energies (both at 350 and 500 GeV) the $e\gamma$ rates are larger. This is clearly due to the effect of the cut in p_T on the spectrum of the photon produced in the initial state of the $e^+e^- \rightarrow \mu^+\mu^- b\bar{b}\gamma$ process, as this latter is clearly harder at higher values of $\sqrt{s}$. The contribution of $b\gamma$–diagrams is generally smaller with respect to the previous ones by at least one order of magnitude, whereas the interference between the three sets is completely negligible. The effect of the `e.m.` radiation on the background is not so promptly identifiable. However, for the distribution in $M_{b\bar{b}}$ one easily recognises the ZZ contribution via the peak at M_Z, which has contributions from γZ too. The $Z\gamma$ and $\gamma\gamma$ crabs have a substantially flat spectrum, the same for the b–`deers`, whereas the μ–`deers` give a $\mathcal{O}(1\%)$ contribution to the Z–peak. In the case of the $M_{b\bar{b}\gamma}$ distribution, the Z–peak has a long tail for $M_{b\bar{b}\gamma} \gtrsim 90$ GeV (such that it practically disappears), due to $b\bar{b}\gamma$ combinations in which the photon does not come from a $Z \rightarrow b\bar{b}\gamma$ decay. The $\gamma\gamma$ `crab` and b–`deer` contributions are small and flat. In general, at NLO, `crabs` are more than one order of magnitude bigger than the `deers`, with the ZZ and γZ largely dominant. Also for this process the (negligible) interferences between signal and background have not been plotted in the figures.

A final remark is needed if one considers that it would generally be impossible to tag photons too close to b–quarks. In fact, partons give rise to jets with a finite angular size, such that if the photon fails within this cone it will not be distinguished from the other parts of the jets. Thus, its energy is counted as part of that one of the hadronic system associated to one of the b–quarks and the $b\bar{b}$ invariant mass is not experimentally measurable for $e^+e^- \rightarrow \mu^+\mu^- b\bar{b}\gamma$ events. Clearly, this frequently happens in the case of diagrams 5–6 in Fig. 2, 5–6 and 12–13 in Fig. 3 and 4. Occasionally, this also occurs for the graphs in which the photon is emitted by lepton lines as well as by b–lines in diagrams 7 & 14 of Fig. 4, when it is collinear with one of the final b's. Whereas in the first case such effect could well be important, we expect it to be rather small in the second one. The overall effect would be that radiative events of the type (2) would look like leading events (1) and that the significance of the signals would be probably improved (as the invariant mass of the hadronic system embodying the untagged photon would now reproduce the Higgs mass, in the case of the mentioned diagrams of Fig. 2). However, in order to correctly predict such an effect one would need to know the terms due to the virtual corrections of the FSR along the b–lines, which are not computed here. An alternative strategy, that we exploit, is to impose an additional cut that forces the photon to be well separated from both b–quarks, for example $\cos\theta_{b\gamma} < 0.95$ (corresponding to a cone with an angular size of ≈ 18 degrees). After applying this additional requirement, we get that in case of the signal the NLO rates are reduced by $\approx 19\%$ at LEP I, and of $\approx 1\%$ and $\approx 4\%$ at a NLC with $\sqrt{s} = 350$ and 500 GeV, respectively. The sum of the background suffers a reduction of $\approx 7(4)[1]\%$ at $\sqrt{s} = 200(350)[500]$ GeV. Therefore, this approach should not drastically modify the significance of hard photon events, al least where these are quantitatively important: that is, at the NLC.

Finally, by integrating the spectra in invariant mass at LO and NLO one obtains that the lowest order rates are generally increased by approximately 12(24)[27]% at $\sqrt{s} = 200(350)[500]$ GeV for the signal, whereas for the background from 18% (at LEP II) to 42(60)% (at the NLC, with $\sqrt{s} = 350(500)$ GeV). However, as we expect that the corrections to the invariant mass spectra due to real photon emission behave quite similarly to those in Figs. 6–8 also in the case $M_H \not\approx M_Z$ (in the range, let us say, 60 GeV $\lesssim M_H \lesssim$ 120 GeV), then, when the peaks of the H– and of the Z–particle are well separated (in the missing mass and/or in the $b\bar{b}$–invariant mass distribution), the inclusion of radiative events in the sample should not change the results that one obtains by an analysis at lowest order (no radiation). Therefore when M_H and M_Z are not degenerate, and the difference $\delta M_{HZ} = M_H - M_Z$ is larger than approximately four times the width of the Z–boson (see, e.g., Ref. [23]), `e.m.` radiative corrections can be safely neglected. On the contrary, for $\delta M_{HZ} \lesssim 4\Gamma_Z$, a full simulation is in principle needed in order to correctly establish the excess of $b\bar{b}$ decays in the $\mu^+\mu^- b\bar{b}(\gamma)$ sample, especially at NLC energies.

4. Summary and conclusions

We have studied next–to–leading order electromagnetic contributions via hard photon radiation to the process $e^+e^- \to \mu^+\mu^- b\bar{b}$, whose signature represents the 'golden channel' to detect and study the intermediate mass Higgs boson of the Standard Model at e^+e^- colliders of the present (LEP II) and future (NLC) generation. In fact, such events involve the production of the Higgs particle via the bremsstrahlung process $e^+e^- \to ZH$ followed by the decays $Z \to \mu^+\mu^-$ and $H \to b\bar{b}$. We restricted our attention to the ZH process only, thus neglecting Higgs production via the $WW-$ and $ZZ-$fusion mechanisms, because of the particular importance of the first one in investigating the properties of the $H-$scalar. We also focused on the case of mass degeneracy $M_H \approx M_Z$. In such conditions, a Higgs signal can be searched for by using b–tagging techniques, to establish in $\mu^+\mu^-b\bar{b}$ samples a content of b–quarks much larger than the one arising from background $Z \to b\bar{b}$ decays only.

Events of the type $e^+e^- \to \mu^+\mu^-b\bar{b}\gamma$ should be included in the phenomenological analysis, because at LEP II and NLC energies the initial state itself produces many hard photons (contrary to LEP I, where their emission is suppressed by the Z–width). Since both muons and b–quarks are charged particles, photons can also be radiated in the final state. As it was not *a priori* clear how this radiation modified the integrated and differential rates of signal and background events and their interplay, it was important to investigate its effects.

Two search strategies have been considered: a missing mass analysis of the system recoiling against the Z–boson identified via the muon pair, and the direct reconstruction of the Higgs peak via the $b\bar{b}$–pair. Whereas for the first procedure the inclusion of hard photons does not modify the M_{recoil} spectra that one gets from the $2 \to 4$ process corrected for soft and collinear ISR, we found that, in the second case, such radiative events give contributions comparable to the differences expected at leading order between the $H \to b\bar{b}$ and the $Z \to b\bar{b}$ rates, for $\sqrt{s} \gtrsim 350$ GeV, when a window around $M_H = 90$ GeV is selected. In particular, NLO contributions are generally larger in the case of the signal, although the overall effect is a slight reduction of the expected relative excess of $b\bar{b}$–pairs from the Higgs decay. At LEP II the influence of higher order corrections is smaller and, in first instance, negligible (in this case NLO rates are even the same for signal and background).

Therefore, in an analysis that uses the direct reconstruction method to disentangle Higgs signals at the NLC and in the region $M_H \approx M_Z$, the next–to–leading order rates should be taken into account, in order to predict correctly the amount of H and Z decays into $b\bar{b}$–pairs. In the case of a missing mass analysis, higher order electromagnetic contributions can be always safely neglected.

For values of M_H different from M_Z, when the peaks of the two particles are well separated, the inclusion of the `e.m.` hard radiation should not change the conclusions one gets at lowest order. The only effect is an overall correction to the normalisations of the differential distributions, which should not drastically modify the significance factors of the signal–to–background analysis.

Before concluding, we remind the reader that our analysis did not make use of a full calculation up to the $\mathcal{O}(\alpha_{em}^5)$ order[19]. Only contributions due to the tree–level $\mathcal{O}(\alpha_{em}^4)$ process $e^+e^- \to \mu^+\mu^- b\bar{b}$ and its $\sim \alpha_{em}$ corrections due to the complete universal ISR (both real and virtual) and to real photon emission from the final state (with $p_T^\gamma > 1$ GeV) have been included here. Therefore, a systematic error related to the ignorance of the virtual FSR effects and of the non factorisable corrections comes with our results. However, we notice that some of these corrections should go in the same direction as our conclusions, that is, of the importance of $\mathcal{O}(\alpha_{em})$ effects on the invariant mass spectra. For example, according to the Kinoshita–Lee–Nauenberg theorem [49], one expects that logarithmic contributions due to 'collinear' emission of photons from the final state must not appear in the expression of the cross sections, these being canceled by the (negative) contributions due to virtual final state photons. In the present paper, the former are included[20] whereas the latter are not: therefore, the size of what we called NLO terms *over*–estimates that of the real $\sim \alpha_{em}$ FSR corrections in the total cross section. Conversely, since such negative terms have the same kinematics as the $2 \to 4$ process, they tend to reduce the LO piece. In particular, the Higgs peaks in the $M_{b\bar{b}}$ distributions should be less pronounced in the end. Thus, neglecting these virtual terms corresponds to somewhat *under*–estimating the effect of hard photon emission on the distributions that are of interest for Higgs searches.

Acknowledgments

We are grateful to Ezio Maina for reading the manuscript and for useful suggestions. This work is supported in part by the Ministero dell' Università e della Ricerca Scientifica, by the UK Particle Physics and Astronomy Research Council and by the EC Programme "Human Capital and Mobility", contract CHRX–CT–93–0357 (DG 12 COMA).

References

[1] G. Altarelli, T. Sjöstrand and F. Zwirner, eds., '*Report of the Workshop on Physics at LEP2*', CERN 96–01 (1996).

[19] Complete QED corrections to four–fermion production are not available yet, although important partial results have been recently presented [48].

[20] At least for the $\mu^+\mu^-$ system, if one implements the cut in $\cos\theta_{b\gamma}$.

[2] Proceedings of the Workshop 'e^+e^- *Collisions at 500 GeV. The Physics Potential*', Munich, Annecy, Hamburg, 3–4 February 1991, ed. P.M. Zerwas, DESY pub. 92–123A/B/C, August 1992.

[3] G. Jackson, talk presented at the Workshop on *Electroweak Symmetry Breaking at TeV-Scale Physics*, UC-Santa Barbara, February 1994.

[4] Proceedings of the '*Large Hadron Collider Workshop*', Aachen, 4–9 October 1990, eds. G. Jarlskog and D. Rein, Report CERN 90–10, ECFA 90–133, Geneva, 1990;
ATLAS Technical Proposal, CERN/LHC/94-43 LHCC/P2 (December 1994);
CMS Technical Proposal, CERN/LHC/94-43 LHCC/P1 (December 1994).

[5] D.R.T. Jones and S.T. Petkov, *Phys. Lett.* **B84** (1979) 440;
R.N. Cahn and S. Dawson, *Phys. Lett.* **B136** (1984) 196;
K. Hikasa, *Phys. Lett.* **B164** (1985) 341;
G. Altarelli, B. Mele and F. Pitolli, *Nucl. Phys.* **B287** (1987) 205;
B. Kniehl, *preprint* DESY 91–128, 1991.

[6] V. Barger, K. Cheung, A. Djouadi, B.A. Kniehl and P.M. Zerwas, *Phys. Rev.* **D49** (1994) 79.

[7] V. Barger, K. Cheung, A. Djouadi, B.A. Kniehl, R.J.N. Phillips and P.M. Zerwas, in Ref. [2].

[8] B.L. Ioffe and V.A. Khoze, *Sov. J. Part. Nucl.* **9** (1978) 50.

[9] J. Ellis, M.K. Gaillard and D.V. Nanopoulos, *Nucl. Phys.* **B106** (1976) 292.

[10] B.W. Lee, C. Quigg and H.B. Thacker, *Phys. Rev.* **D16** (1977) 1519.

[11] F.A. Berends and R. Kleiss, *Nucl. Phys.* **B260** (1985) 32.

[12] M. Consoli, W.F.L. Hollik and F. Jegerlehner, in '*Z Physics at LEP 1*', ed. by G. Altarelli, R. Kleiss and C. Verzegnassi, CERN Yellow Report No. 89-08 (1989), Vol. 1, page 7;
W.F.L. Hollik, *Fortschr. Phys.* **38** (1990) 165.

[13] Z. Hioki, *Phys. Lett.* **B224** (1989) 417.

[14] B.A. Kniehl, *Phys. Lett.* **B282** (1992) 249.

[15] J. Fleischer and F. Jegerlehner, *Nucl. Phys.* **B216** (1983) 469;
B.A. Kniehl, *Z. Phys.* **C55** (1992) 605;
A. Denner, J. Kublbeck, R. Mertig and M. Böhm, *Z. Phys.* **C56** (1992) 261.

[16] E. Gross, G. Wolf and B.A. Kniehl, *Z. Phys.* **C63** (1994) 417; Erratum, *ibidem* **C66** (1995) 321.

[17] P. Nogueira and J.C. Romão, *Z. Phys.* **C60** (1993) 757.

[18] D. Bardin, A. Leike and T. Riemann, *Phys. Lett.* **B344** (1995) 383.

[19] D. Bardin, A. Leike and T. Riemann, in Proc. of the '*Zeuthen Workshop on Elementary Particle Theory - Physics at LEP 200 and Beyond*', ed. by T. Riemann and J. Blümlein, Teupitz, Germany, April 1994, *Nucl. Phys.* **B37** (1994) 274 (Proc. Suppl.).

[20] D. Bardin, A. Leike and T. Riemann, *Phys. Lett.* **B353** (1995) 513.

[21] E. Boos, M. Sachwitz, H.J. Schreiber and S. Shichanin, *Z. Phys* **C61** (1994) 675; *ibidem* **C64** (1994) 391; *ibidem* **C67** (1995) 613; *Int. J. Mod. Phys.* **A10** (1995) 2067;
M. Dubinin, V. Edneral, Y. Kurihara and Y. Shimitzu, *Phys. Lett.* **B329** (1994) 379;
F.A. Berends, R. Kleiss and R. Pittau, *Nucl. Phys.* **B424** (1994) 308; *ibidem* **B426** (1994) 344; *Comput. Phys. Commun.* **85** (1995) 437.

[22] G. Passarino, *preprint* hep-ph/9602302, February 1996;
G. Montagna, O. Nicrosini, G. Passarino and F. Piccinini, *Phys. Lett.* **B348** (1995) 178.

[23] P. Grosse-Wiesmann, D. Haidt and H.J. Schreiber, in Ref. [2].

[24] S. Moretti, *preprint* DFTT 40/95, DTP/95/58, June 1995 (to be published in *Z. Phys.* **C**).

[25] A. Ballestrero, E. Maina and S. Moretti, *Phys. Lett.* **B335** (1994) 460.

[26] T. Barklow, P. Chen and W. Kozanecki, in Ref. [2].

[27] F.A. Berends, W.L. van Neerven and G.J. Burgers, *Nucl. Phys.* **B297** (1988) 429; Erratum, *ibidem* **B304** (1988) 95;
E.A. Kuraev and V.S. Fadin, *Sov. J. Nucl. Phys.* **41** (1985) 466;

G. Altarelli and G. Martinelli, Proceedings of the Workshop '*Physics at LEP*', eds. J. Ellis and R. Peccei, Gèneva, 1986, CERN 86-02;
R. Kleiss, *Nucl. Phys.* **B347** (1990) 29.

[28] O. Nicrosini and L. Trentadue, *Phys. Lett.* **B196** (1987) 551; *Z. Phys.* **C39** (1988) 479.

[29] J. Fleischer, F. Jegerlehner, K. Kolodziej and G. J. van Oldenborgh, *Comp. Phys. Comm.* **85** (1994) 29.

[30] G. J. van Oldenborgh, *preprint* INLO-PUB-95/04, March 1995, revised October 1995.

[31] F.A. Berends, R. Kleiss and R. Pittau, *Nucl. Phys.* **B424** (1994) 308;
D. Bardin, M. Bilenky, D. Lehner, A. Olchevski and T. Riemann, in Proceedings of the '*Zeuthen Workshop on Elementary Particle Theory: Physics al LEP 200 and Beyond*', eds. T. Riemann and J. Blümlein, *Nucl. Phys.* **37B** (1994) 148 (Proc. Suppl.).

[32] D. Bardin, D. Lehner and T. Riemann, *preprint* DESY 96–028, February 1996.

[33] W. Beenakker, K. Kolodziej and T. Sack, *Phys. Lett.* **B258** (1991) 469;
W. Beenakker, F.A. Berends and T. Sack, *Nucl. Phys.* **B367** (1991) 287;
J. Fleischer, F. Jegerlehner and K. Kolodziej, *Phys. Rev.* **D476** (1993) 830.

[34] W. Beenakker, in Proceedings of the '*Zeuthen Workshop on Elementary Particle Theory: Physics al LEP 200 and Beyond*', eds. T. Riemann and J. Blümlein, *Nucl. Phys.* **37B** (1994) 59 (Proc. Suppl.).

[35] V.S. Fadin, V.A. Khoze and A.D. Martin, *Phys. Lett.* **B311** (1993) 311; *ibidem* **B320** (1994) 141; *Phys. Rev.* **D49** (1994) 2247.

[36] M. Böhm, A. Denner, T. Sack, W. Beenakker, F.A. Berends and H. Kuijf, *Nucl. Phys.* **B304** (1988) 463;
J. Fleisher F. Jegerlehner and M. Zralek, *Z. Phys.* **C42** (1989) 409.

[37] T. Stelzer and W.F. Long, *Comp. Phys. Comm.* **81** (1994) 357.

[38] H. Murayama, I. Watanabe and K. Hagiwara, HELAS: HELicity Amplitude Subroutines for Feynman Diagram Evaluations, *KEK Report* 91-11, January 1992.

[39] G.P. Lepage, *Jour. Comp. Phys.* **27** (1978) 192.

[40] S. Moretti, *preprint* DFTT 69/94, DTP/95/02, December 1994 (to be published in *Phys. Rev.* **D**).

[41] E. Braaten and J.P. Leveille, *Phys. Rev.* **D22** (1980) 715;
N. Sakai, *Phys. Rev.* **D22** (1980) 2220;
T. Inami and T. Kubota, *Nucl. Phys.* **B179** (1981) 171;
M. Drees and K. Hikasa, *Phys. Lett.* **B240** (1990) 455;
S.G. Gorishny, A.L. Kataev, S.A. Larin and L.R. Surguladze, *Mod. Phys. Lett.* **A5** (1990) 2703;
L.R. Surguladze, *Phys. Lett.* **B341** (1994) 60.

[42] Z. Kunszt and W.J. Stirling, *Phys. Lett.* **B242** (1990) 507;
N. Brown, *Z. Phys.* **C49** (1991) 657;
V. Barger and K. Whisnant, *Phys. Rev.* **D43** (1991) 1443.

[43] CDF Collaboration, *Phys. Rev. Lett.* **74** (1995) 2626.

[44] D0 Collaboration, *Phys. Rev. Lett.* **74** (1995) 2632.

[45] A. Ballestrero, E. Maina and S. Moretti, *Phys. Lett.* **B333** (1994) 434.

[46] See for example:
W. Bernreuther *et al.*, in Ref. [2], and References therein.

[47] G. Bagliesi *et al.*, in Ref. [2].

[48] See for example:
W. Beenakker *et al.*, *Report of the Working Group on WW Cross Sections and Distributions*, in Ref. [1], and References therein;
D. Bardin *et al.*, *Report of the Working Group on Event Generators for WW Physics*, in Ref. [1], and References therein;
F. Boudjema *et al.*, *Report of the Working Group on Standard Model Processes*, in Ref. [1], and References therein;
M.L. Mangano *et al.*, *Report of the Working Group on Event Generators for Discovery Physics*, in Ref. [1], and References therein.

[49] T. Kinoshita, *J. Math. Phys.* **3** (1962) 650;
T.D. Lee and M. Nauenberg, *Phys. Rev.* **133B** (1964) 1549.

Table Captions

Tab. I Cross sections in femtobarns in the window $|M_{b\bar{b}(\gamma)} - M_H| < 10$ GeV (being $M_H =$ 90 GeV), after the cuts: $p_T^{\mu,b} > 1$ GeV, $|M_{\mu^+\mu^-} - M_Z| < 10$ GeV and $|\cos\theta_{\mu^+\mu^-}| < 0.8$, for signal ($S$) and background ($B$), together with the total significance Σ (see page 10–11 in the text for their definitions), for the integrated luminosity $\mathcal{L} = 0.5$ fb^{-1}. The label LO refers to the rates of the leading process (1) corrected for the ISR due to soft, collinear and virtual photons, whereas the label NLO identifies those from process (2) with hard photons ($p_T^\gamma > 1$ GeV). The second line for NLO events represents rates derived from the distributions in $M_{b\bar{b}\gamma}$, whereas the others refer to cross sections and significances obtained from the $M_{b\bar{b}}$ spectra. The CM energy is $\sqrt{s} = 200$ GeV.

Tab. II Same as Tab. I, with $\sqrt{s} = 350$ GeV and $\mathcal{L} = 20$ fb^{-1}.

Tab. III Same as Tab. I, with $\sqrt{s} = 500$ GeV and $\mathcal{L} = 20$ fb^{-1}.

Figure Captions

Fig. 1 Feynman diagrams at tree–level for the process $e^+e^- \to \mu^+\mu^- b\bar{b}$ (with the labelling: e^+ (1), e^- (2), μ^+ (3), μ^- (4), b (5) and $\bar{b}$ (6)): a) `crabs`; b) μ–`deers`; c) b–`deers` and d) the signal ZH. Internal wavy lines represent a γ or a Z in the case of the graphs a, b and c, whereas for the signal they represent a Z only. Permutations of the virtual boson lines along the fermion ones are not shown.

Fig. 2 Feynman diagrams at tree–level for the process $e^+e^- \to \mu^+\mu^- b\bar{b}\gamma$ (with the labelling: e^+ (1), e^- (2), μ^+ (3), μ^- (4), b (5), $\bar{b}$ (6) and γ (7)) in the case of the signal ZH. Internal wavy lines represent a Z.

Fig. 3 Feynman diagrams at tree–level for the process $e^+e^- \to \mu^+\mu^- b\bar{b}\gamma$ (with the labelling: e^+ (1), e^- (2), μ^+ (3), μ^- (4), b (5), $\bar{b}$ (6) and γ (7)) in the case of the `crabs`. Internal wavy lines represent a γ or a Z.

Fig. 4 Feynman diagrams at tree–level for the process $e^+e^- \to \mu^+\mu^- b\bar{b}\gamma$ (with the labelling: e^+ (1), e^- (2), μ^+ (3), μ^- (4), b (5), $\bar{b}$ (6) and γ (7)) in the case of the `deers`. Labels $i[i]$ (for $i = 3, 4, 5$ and 6) identify the $b[\mu]$–`deer` contributions. Internal wavy lines represent a γ or a Z.

Fig. 5 Distribution in the invariant mass of the $b\bar{b}$–pair ($M_{b\bar{b}}$) in non–radiative $e^+e^- \to \mu^+\mu^- b\bar{b}$ events, for signal (shaded) and background (see page 10 in the text for their definitions), for $M_H = 90$ GeV, $\sqrt{s} = 200$ GeV (a), $\sqrt{s} = 350$ GeV (b) and $\sqrt{s} = 500$ GeV (c), after the sequence of cuts: $p_T^{\mu,b} > 1$ GeV, $|M_{\mu^+\mu^-} - M_Z| < 10$ GeV and $|\cos\theta_{\mu^+\mu^-}| < 0.8$.

Fig. 6 Distribution in the invariant mass of the $b\bar{b}$– ($M_{b\bar{b}}$, a) and of the $b\bar{b}\gamma$–system ($M_{b\bar{b}\gamma}$, b) in $e^+e^- \to \mu^+\mu^- b\bar{b}\gamma$ events, for signal (shaded) and background (see page 10 in the text for their definitions), for $M_H = 90$ GeV and $\sqrt{s} = 200$ GeV, after the sequence of cuts: $p_T^{all} > 1$ GeV, $|M_{\mu^+\mu^-} - M_Z| < 10$ GeV and $|\cos\theta_{\mu^+\mu^-}| < 0.8$.

Fig. 7 Same as Fig. 6, with $\sqrt{s} = 350$ GeV.

Fig. 8 Same as Fig. 6, with $\sqrt{s} = 500$ GeV.

$e^+e^- \rightarrow \mu^+\mu^- b\bar{b}(\gamma)$						
S (fb)	B (fb)	Σ				
		$\epsilon_b = 0.2$	$\epsilon_b = 0.4$	$\epsilon_b = 0.6$	$\epsilon_b = 0.8$	$\epsilon_b = 1.0$
10.0[14.4]	6.17[8.92]	1.55[1.87]	2.01[2.45]	2.32[2.78]	2.44[2.92]	2.85[3.42]
LO[no radiation]						
1.13	1.10	1.59	2.10	2.38	2.51	2.92
0.94	0.92	1.58	2.10	2.37	2.50	2.91
NLO						
$\vert M_{b\bar{b}(\gamma)} - M_H\vert < 10$ GeV $\quad p_T^{\mu,b} > 1$ GeV						
$\vert M_{\mu^+\mu^-} - M_Z\vert < 10$ GeV $\quad \vert\cos\theta_{\mu^+\mu^-}\vert < 0.8$						
$\sqrt{s} = 200$ GeV $\quad M_H = 90$ GeV $\quad \mathcal{L} = 0.5$ fb^{-1}						

Tab. I

$e^+e^- \to \mu^+\mu^- b\bar{b}(\gamma)$						
S (fb)	B (fb)	Σ				
		$\epsilon_b = 0.2$	$\epsilon_b = 0.4$	$\epsilon_b = 0.6$	$\epsilon_b = 0.8$	$\epsilon_b = 1.0$
4.04[4.79]	1.53[1.94]	7.94[8.35]	10.5[11.0]	11.9[12.5]	12.5[13.2]	14.6[15.4]
LO[no radiation]						
0.95	0.66	8.21	10.9	12.3	12.9	15.1
0.29	0.17	8.06	10.7	12.1	12.7	14.8
NLO						
$\|M_{b\bar{b}(\gamma)} - M_H\| < 10$ GeV				$p_T^{\mu,b} > 1$ GeV		
$\|M_{\mu^+\mu^-} - M_Z\| < 10$ GeV				$\|\cos\theta_{\mu^+\mu^-}\| < 0.8$		
$\sqrt{s} = 350$ GeV			$M_H = 90$ GeV		$\mathcal{L} = 20$ fb^{-1}	

Tab. II

$e^+e^- \to \mu^+\mu^- b\bar{b}(\gamma)$						
S (fb)	B (fb)	Σ				
		$\epsilon_b = 0.2$	$\epsilon_b = 0.4$	$\epsilon_b = 0.6$	$\epsilon_b = 0.8$	$\epsilon_b = 1.0$
1.89[2.12]	0.62[0.79]	5.80[5.78]	7.68[7.63]	8.70[8.65]	9.16[9.11]	10.7[10.6]
LO[no radiation]						
0.51	0.38	5.80	7.67	8.68	9.15	10.7
0.094	0.064	5.81	7.68	8.69	9.16	10.7
NLO						
$\vert M_{b\bar{b}(\gamma)} - M_H\vert < 10$ GeV $p_T^{\mu,b} > 1$ GeV						
$\vert M_{\mu^+\mu^-} - M_Z\vert < 10$ GeV $\vert\cos\theta_{\mu^+\mu^-}\vert < 0.8$						
$\sqrt{s} = 500$ GeV $M_H = 90$ GeV $\mathcal{L} = 20$ fb^{-1}						

Tab. III

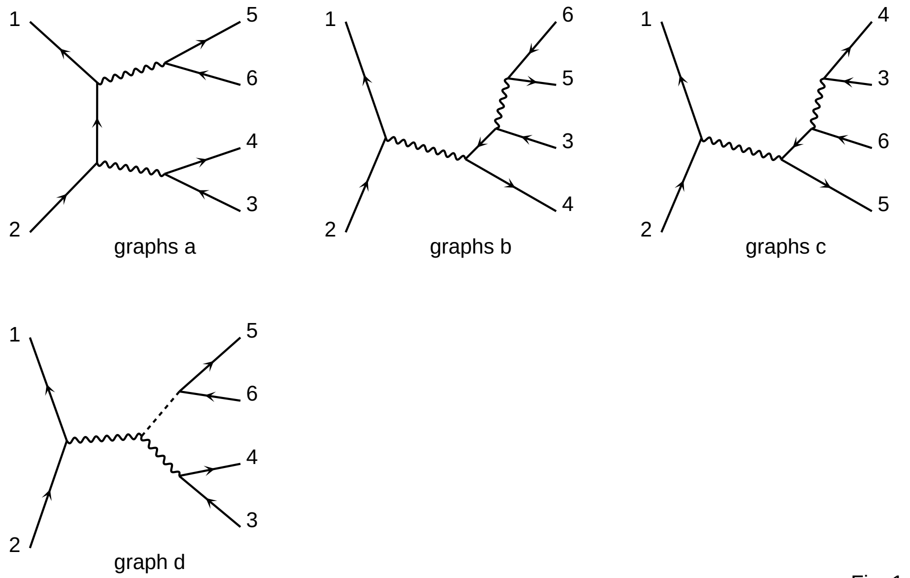
1
5
6
4
3
2
graphs a
1
6
5
3
4
2
graphs b
1
4
3
6
5
2
graphs c
1
5
6
4
3
2
graph d

Fig. 1

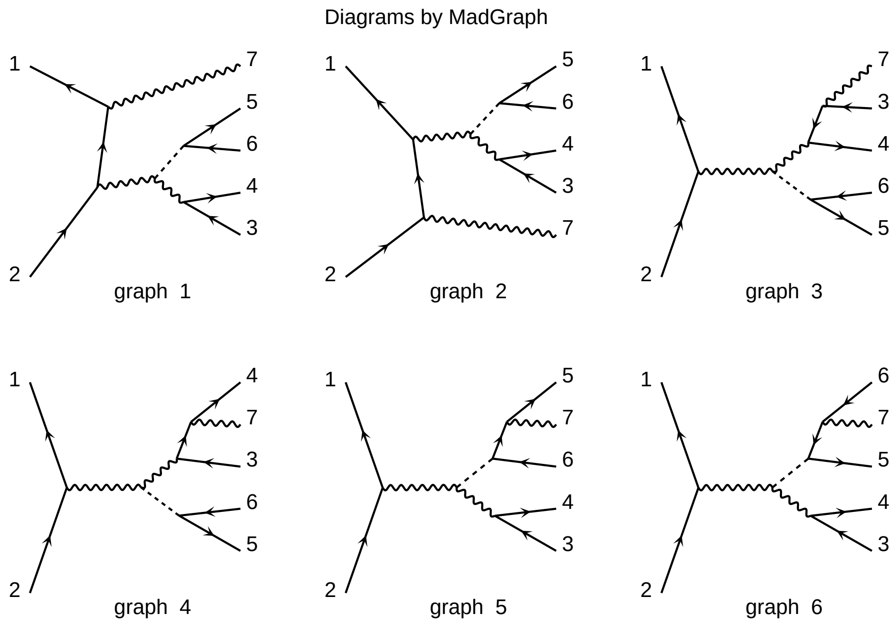
Diagrams by MadGraph
1 2 7 5 6 4 3
graph 1
1 2 5 6 4 3 7
graph 2
1 2 7 3 4 6 5
graph 3
1 2 4 7 3 6 5
graph 4
1 2 5 7 6 4 3
graph 5
1 2 6 7 5 4 3
graph 6

Fig. 2

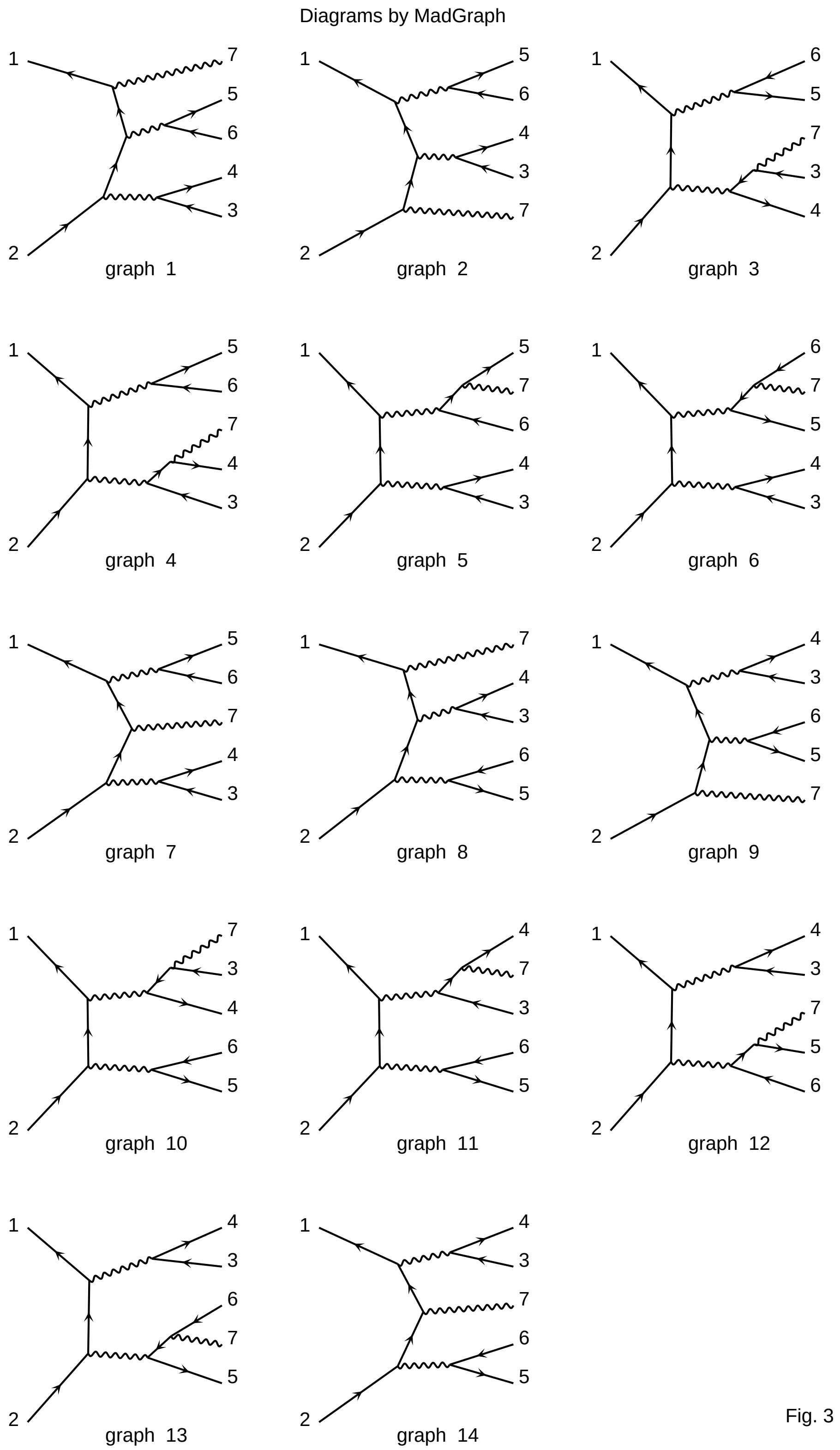
Diagrams by MadGraph
graph 1
graph 2
graph 3
graph 4
graph 5
graph 6
graph 7
graph 8
graph 9
graph 10
graph 11
graph 12
graph 13
graph 14

Fig. 3

Diagrams by MadGraph

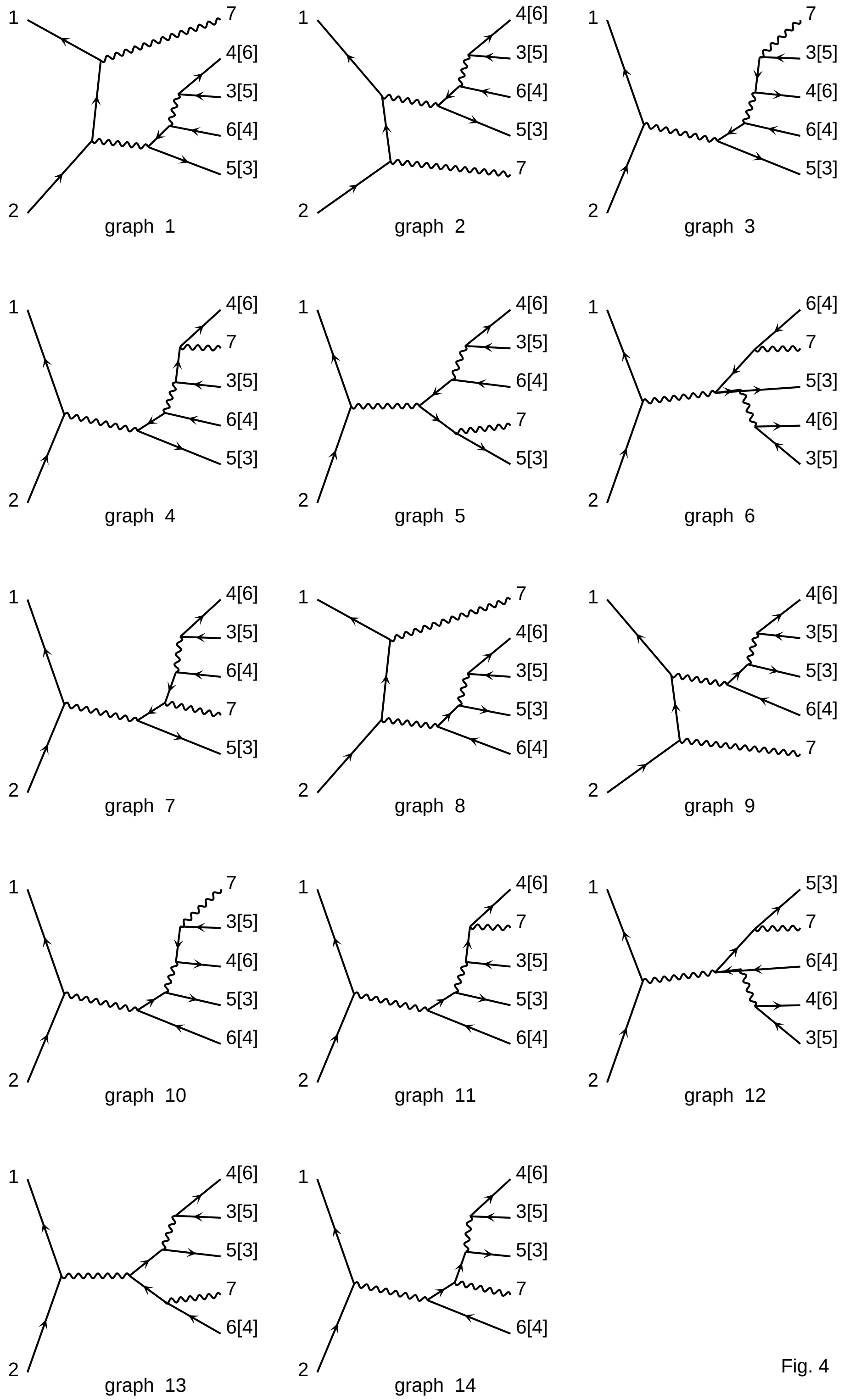

Fig. 4

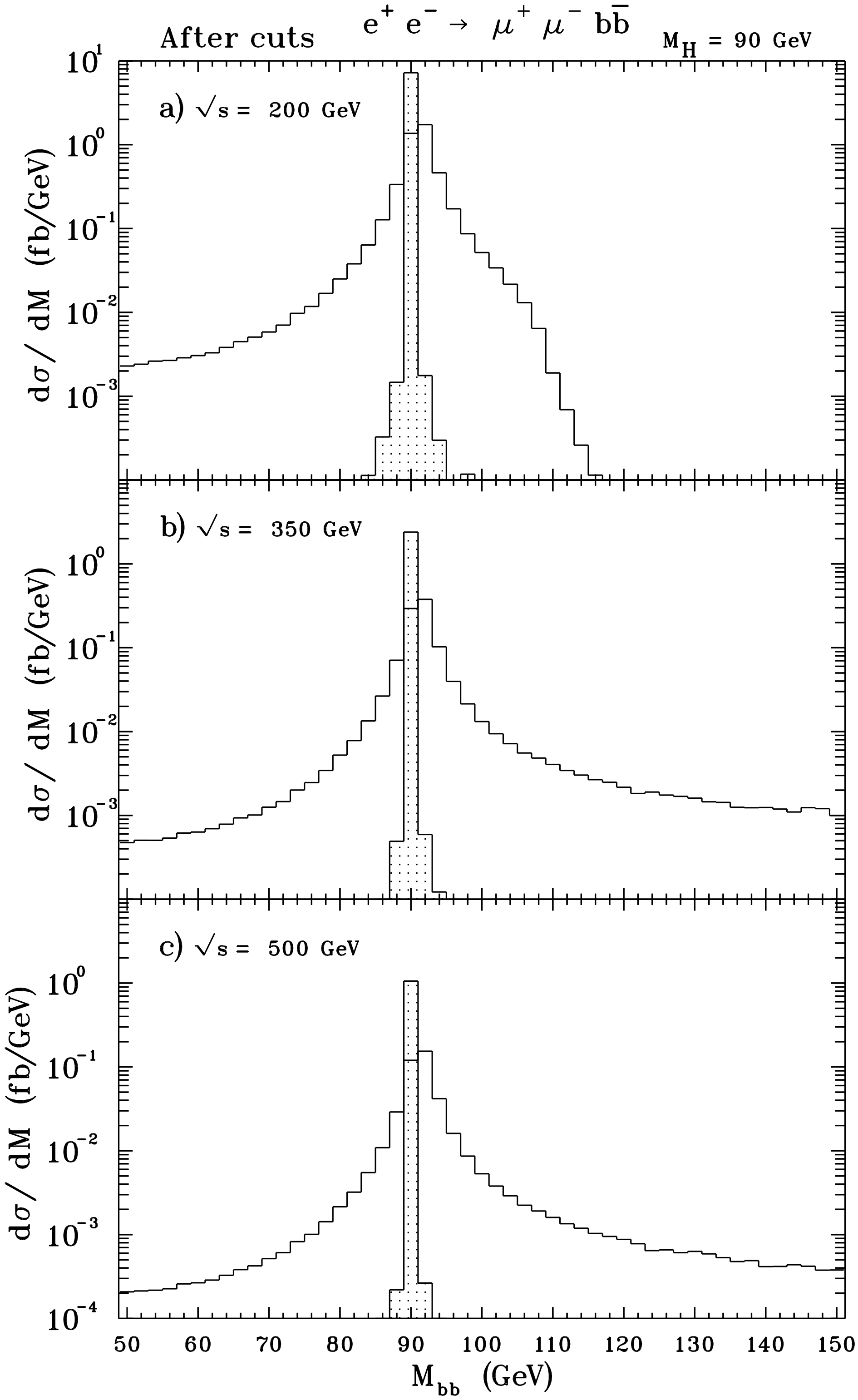
After cuts
$e^+ e^- \to \mu^+ \mu^- b\bar{b}$
M_H = 90 GeV
a) $\sqrt{s}$ = 200 GeV
b) $\sqrt{s}$ = 350 GeV
c) $\sqrt{s}$ = 500 GeV
$d\sigma$ / dM (fb/GeV)
10^{1}
10^{0}
10^{-1}
10^{-2}
10^{-3}
10^{-4}
50
60
70
80
90
100
110
120
130
140
150
M_{bb} (GeV)

Fig. 5

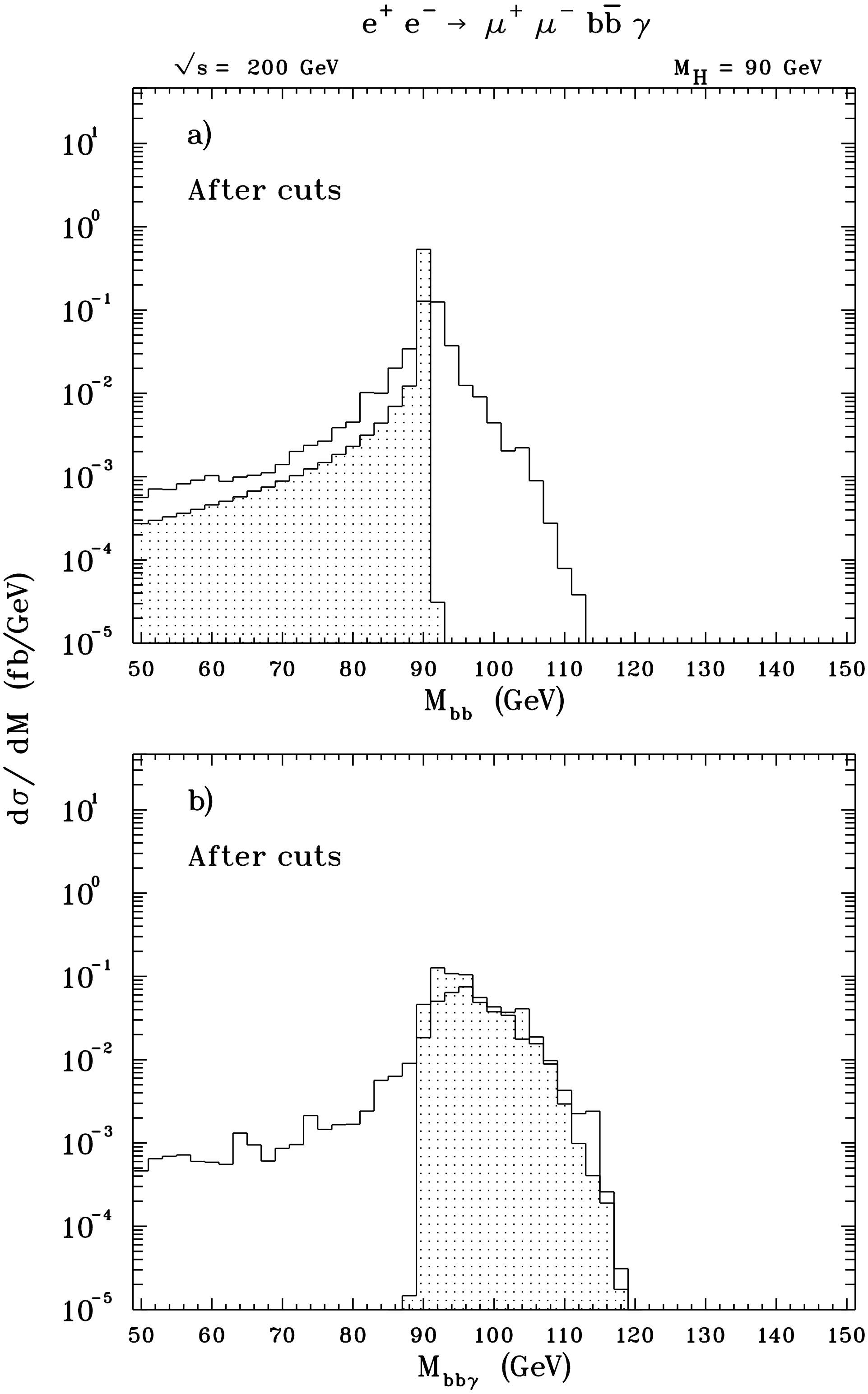

$e^+ e^- \to \mu^+ \mu^- b\bar{b}\, \gamma$
$\sqrt{s} = 200$ GeV
$M_H = 90$ GeV
a)
After cuts
$d\sigma / dM$ (fb/GeV)
M_{bb} (GeV)
b)
After cuts
$M_{bb\gamma}$ (GeV)

Fig. 6

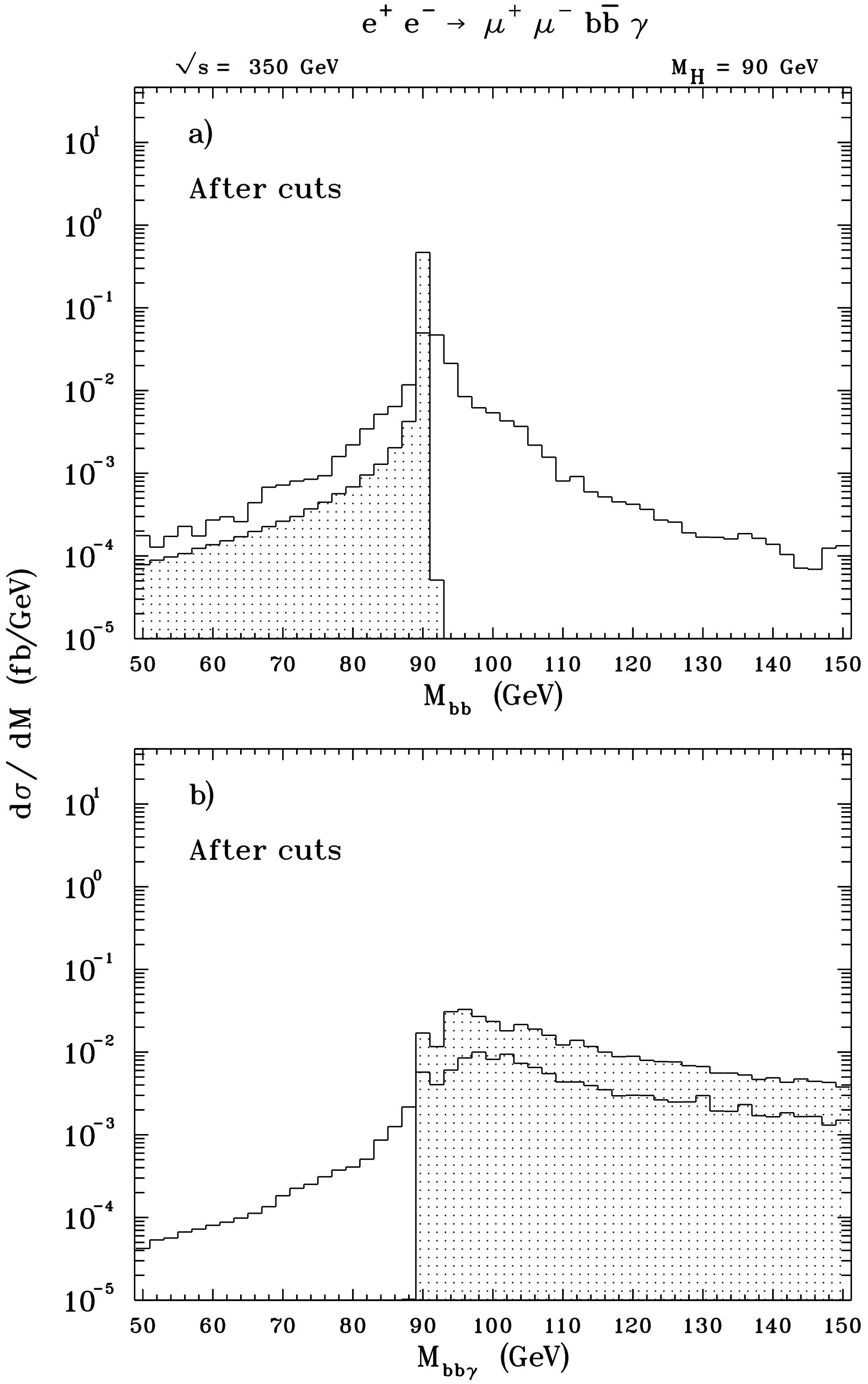

e+ e− → μ+ μ− bb̄ γ
√s = 350 GeV
M_H = 90 GeV
dσ/ dM (fb/GeV)
a)
After cuts
10^1
10^0
10^-1
10^-2
10^-3
10^-4
10^-5
50 60 70 80 90 100 110 120 130 140 150
M_bb (GeV)
b)
After cuts
M_bbγ (GeV)

Fig. 7

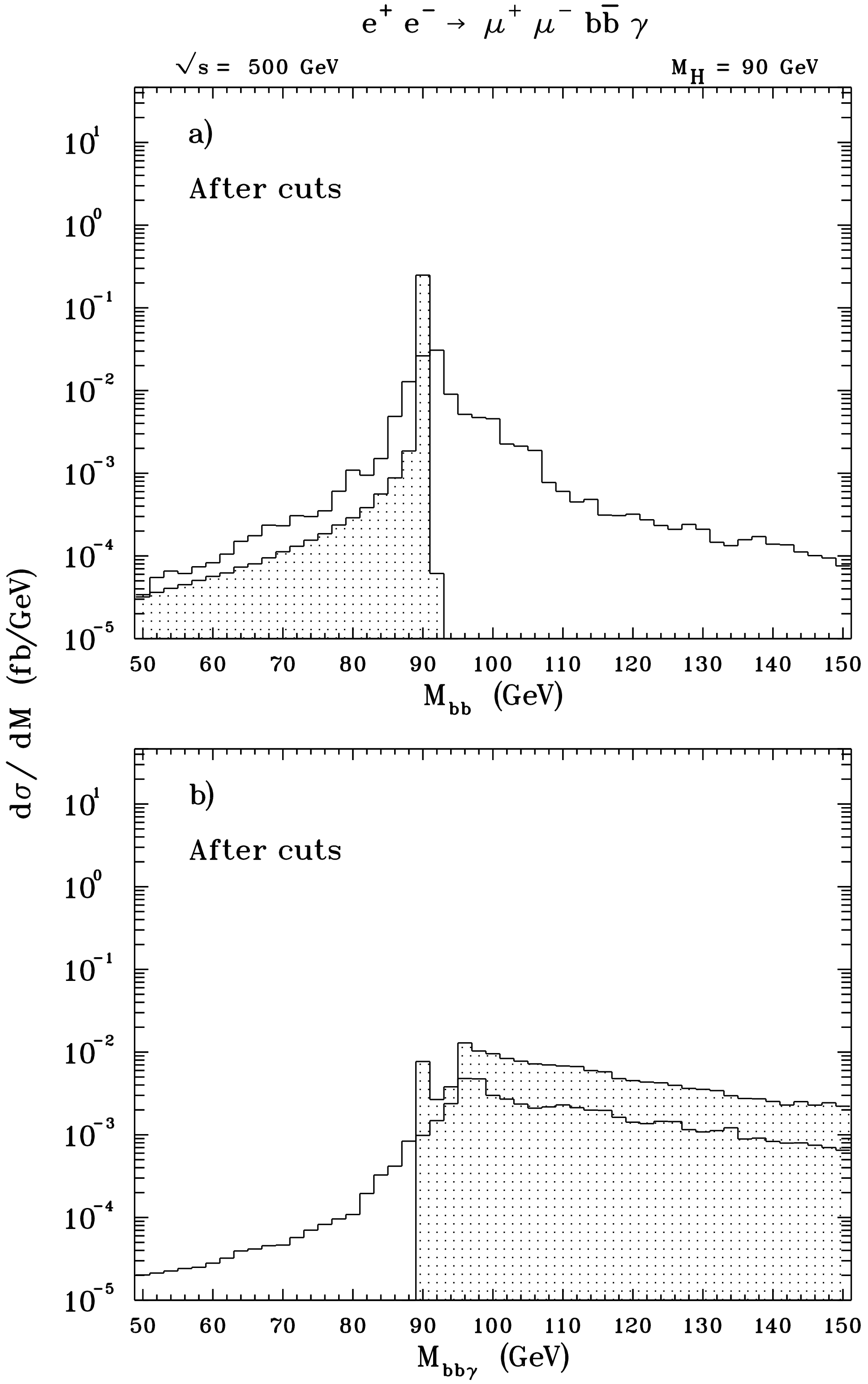

e+ e− → μ+ μ− bb̄ γ
√s = 500 GeV
M_H = 90 GeV
a)
After cuts
b)
After cuts
dσ / dM (fb/GeV)
M_bb (GeV)
M_bbγ (GeV)

Fig. 8